DropBot: An open-source digital microfluidic control system with precise control of electrostatic driving force and instantaneous drop velocity measurement

Ryan Fobel, Christian Fobel, and Aaron R. Wheeler

Articles you may be interested in

Digital control of force microscope cantilevers using a field programmable gate array
Rev. Sci. Instrum. **79**, 123705 (2008); 10.1063/1.3043432

Development of an isothermal titration microcalorimetric system with digital control and dynamic power peltier compensation. II. Characterization and operation mode. Myoglobin adsorption onto polymeric latex particles
Rev. Sci. Instrum. **71**, 1832 (2000); 10.1063/1.1150544

Development of an isothermal titration microcalorimetric system with digital control and dynamic power Peltier compensation. I. Description and basic performance
Rev. Sci. Instrum. **71**, 1824 (2000); 10.1063/1.1150543

A digital control system for the iodine stabilized He–Ne laser
Rev. Sci. Instrum. **69**, 1934 (1998); 10.1063/1.1148875

A novel digital feedback scheme of shear-force control in near-field scanning optical microscopy
Rev. Sci. Instrum. **68**, 2783 (1997); 10.1063/1.1148195

DropBot: An open-source digital microfluidic control system with precise control of electrostatic driving force and instantaneous drop velocity measurement

Ryan Fobel,[1,2] Christian Fobel,[3] and Aaron R. Wheeler[1,2,4,a]

[1]*Institute for Biomaterials and Biomedical Engineering, University of Toronto, 164 College St., Toronto, Ontario M5S 3G9, Canada*
[2]*Donnelly Centre for Cellular and Biomolecular Research, 160 College St., Toronto, Ontario M5S 3E1, Canada*
[3]*School of Computer Science, University of Guelph, 50 Stone Road East, Guelph, Ontario N1G 2W1, Canada*
[4]*Department of Chemistry, University of Toronto, 80 St. George St., Toronto, Ontario M5S 3H6, Canada*

We introduce DropBot: an open-source instrument for digital microfluidics (http://microfluidics.utoronto.ca/dropbot). DropBot features two key functionalities for digital microfluidics: (1) real-time monitoring of instantaneous drop velocity (which we propose is a proxy for resistive forces), and (2) application of constant electrostatic driving forces through compensation for amplifier-loading and device capacitance. We anticipate that this system will enhance insight into failure modes and lead to new strategies for improved device reliability, and will be useful for the growing number of users who are adopting digital microfluidics for automated, miniaturized laboratory operation. © 2013 AIP Publishing LLC. [http://dx.doi.org/10.1063/1.4807118]

Digital Microfluidics (DMF) is an emerging fluid-handling technology that allows for precise control of individually addressable drops on an array of electrodes using electrostatic forces.[1–3] Primary benefits of DMF over macro-scale techniques include reduced sample and reagent volumes and amenability to automation. In the past decade, DMF has been applied to a range of problems in biology, chemistry, and medicine,[4,5] but widespread adoption of this technology requires improvements in device robustness and experimental reproducibility. In response to this challenge, we present DropBot: an open-source instrument for controlling drop actuation in digital microfluidics. DropBot features two unique functionalities, both useful improving device robustness and reproducibility: (1) real-time monitoring of instantaneous drop velocity, and (2) application of a precise electrostatic driving force regardless of device-specific properties.

The first functionality, measurement of instantaneous velocity, is intrinsically linked to the sensitivity of drop movement to device surface variability. Small imperfections (e.g., scratches or dust) or the adsorption of proteins or other biomolecules can make it difficult to move liquids over extended periods; this is especially true for devices operated in air (as opposed to oil). While there has been significant progress in extending operation lifetimes (e.g., using Pluronic additives[6,7] and closed-loop control[8,9]), the prospect for subsequent improvements would be greatly enhanced by a tool for quantitatively measuring the impact of various strategies. Under a given applied force, we assume that an increase in resistive forces will result in a corresponding reduction in drop velocity; therefore, we propose that instantaneous drop velocity should provide a useful proxy for the resistive forces experienced by a drop on a DMF device. We contrast the *instantaneous* velocity, which can be measured for an individual drop as it translates onto each individual electrode, from the *average* velocity which can be measured for a drop after moving over many electrodes; both concepts are useful, but only the former is useful for probing local surface heterogeneities, which is critical for reliable DMF operation. Image-based methods[2,10,11] are capable of measuring instantaneous drop velocity, but obtaining sufficient time-resolution requires expensive high-speed cameras and significant computational resources, making real-time measurements impractical. Furthermore, optical systems impose strict constraints on visual contrast and lighting. Thus, we propose that a more general solution is to use electrical impedance-based sensing,[8,9,12–20] which has been used previously to evaluate drop location[8,9,19,20] and average drop velocity.[8] Unfortunately, measuring impedance *during* drop translation (necessary for estimating instantaneous velocity) is more technically challenging because of the required dynamic range and considerations for parasitic capacitance. DropBot is unique in that it allows for instantaneous velocity measurements during drop movement, which leads us to interesting observations on voltage-driven surface modification.

The second functionality is the application of precise and reproducible actuation forces. This has not been achievable in systems reported previously because of complications arising from amplifier-loading and variability in device capacitance. Amplifier-loading refers to the sensitivity of output voltage to the impedance of the load attached to an amplifier. This problem is exacerbated by automated systems relying on solid-state switches because the switches themselves contribute a significant capacitive load to the system. The second factor limiting the reliable application of DMF driving forces is variability in device capacitance as a function of differences in the thickness and dielectric constant of the insulating layer. Dielectric thickness may vary batch-to-batch in fabrication or even across a given device if the layer

---

a)Electronic mail: aaron.wheeler@utoronto.ca

is applied unevenly. The force responsible for translating drops is related to capacitance by[21–23]

$$F_{actuation} = \frac{1}{2}LcV^2,$$ (1)

where L is electrode width, c is capacitance per unit area, and V is actuation voltage; therefore, variability in device capacitance requires adjustment of the actuation voltage to maintain a consistent force. In all systems reported previously, operators have had to adjust the voltage for each condition; however, this requires manual intervention and limits the ability to make meaningful comparisons across devices and experiments. DropBot allows for automated, real-time tuning of applied potentials to maintain constant driving forces for devices that are radically different in composition.

An overview of the DropBot system and a screenshot of the graphical user interface are shown in Fig. 1. Users can activate/deactivate electrodes on the DMF device by mouse-clicking on the webcam video overlay, providing an intuitive interface with real-time visual feedback. In addition, sequences of actuation steps can be pre-programmed, enabling fully automated operation. The system is based on an Arduino Mega 2560 (SmartProjects, Italy) microcontroller board and houses a custom circuit for measuring device impedance and amplifier output (a simplified version of this circuit is shown in Fig. 2(a)). Source code and circuit schematics are available at http://microfluidics.utoronto.ca/dropbot, and detailed experimental methods are included in the online supplementary material.[26]

The DropBot system continuously monitors the amplifier output and device impedance to maintain a stable actuation voltage and to track the position and velocity of drops. Accurate measurements of these parameters are critical to automated DMF operation, but in each case, we have observed that parasitic capacitance introduces a significant bias. The problem of parasitic capacitance in automated DMF systems has never before been addressed, and we believe that this has limited the precision and reproducibility obtainable with previously reported systems.

In the absence of parasitic capacitance, a voltage divider comprising a 10 MΩ resistor in series with a reference resistor (either $R_{hv0} = 100$ kΩ or $R_{hv1} = 1$ MΩ) should provide frequency-independent attenuation of 11- or 101-fold. The ability to switch between these two attenuation levels facilitates an increased signal-to-noise ratio over a wide dynamic range. The amplifier output is estimated from V_{hv} using the following equation:
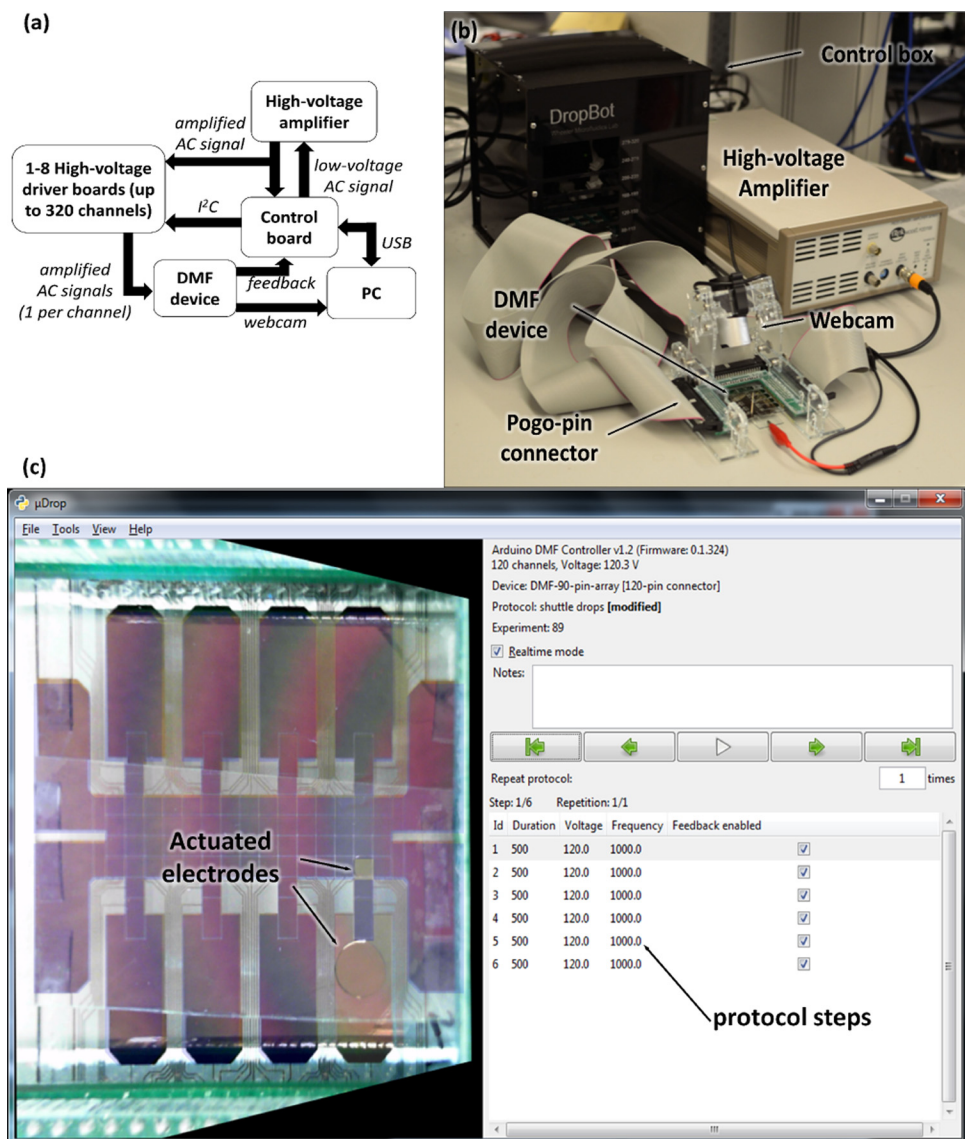

FIG. 1. The DropBot DMF automation system. (a) Block diagram. (b) Photograph of the DropBot system (which contains an Arduino-based control board and up to eight 40-channel high-voltage driver boards) connected to a high-voltage amplifier and a pogo-pin DMF device interface. (c) Screenshot from the custom PYTHON software demonstrating live video overlay.
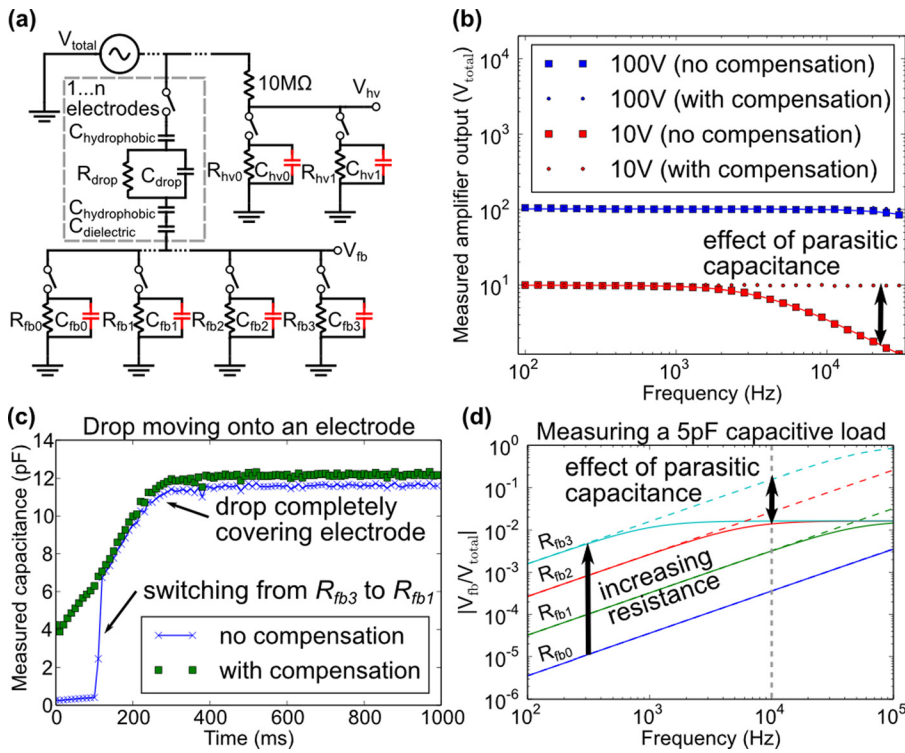
FIG. 2. Impedance and amplifier output measurement. (a) Circuit schematic including parasitic capacitance (red). The gray dashed box contains the circuit model for a drop on a single actuation electrode. (b) Measurements of the amplifier output for 100 V_{rms} (blue) and 10 V_{rms} (red) signals, both with compensation for parasitic capacitance (dots) and without (squares). Solid lines represent the models used to apply the correction. (c) Device capacitance as a function of time as a drop is moving onto an actuated electrode with compensation (green squares) and without (blue markers). A solid blue line is used to guide the eye. (d) Simulation of the theoretical attenuation of the total voltage by each of the four feedback resistors (R_{fb0}-dark blue, R_{fb1}-green, R_{fb2}-red, R_{fb3}-light blue). Dashed lines represent attenuation in the absence of parasitic capacitance, while solid lines include capacitive effects. The vertical gray dashed line corresponds to the frequency applied in c, showing the effect of parasitic capacitance on measurements made with R_{fb3}.

$$V_{total} = V_{hv}\sqrt{\left(1 + \frac{10^6}{R_{hvi}}\right)^2 + (2\pi 10^6 C_{hvi}f)^2}, \quad (2)$$

where R_{hvi} is the reference resistance and C_{hvi} is the parasitic capacitance when resistor i is selected, and f is the frequency in Hz. The results using this approach are shown in the "no compensation" data (square boxes) in Fig. 2(b), where C_{hvi} is assumed to be equal to zero. At high frequencies, the 10 V (measured with R_{hv0}) and 100 V (measured with R_{hv1}) signals deviate from their expected values, consistent with a first-order low-pass filter (the capacitive element arises from the parasitic capacitance of the resistor, copper traces, etc.). By experimentally measuring and including this capacitive term in Eq. (2), the expected signals are recovered.

Parasitic capacitance also impacts the estimation of device capacitance, as demonstrated in Fig. 2(c). Initially, there is little liquid on the active electrode; therefore, the current passing through the device is low and the largest feedback resistor, R_{fb3}, is required to obtain sufficient sensitivity. V_{fb} increases as the drop moves onto the electrode, and before it surpasses 5 V, R_{fb3} is swapped for the smaller R_{fb1}. This change in resistors at $t \approx 100$ ms produces a discontinuity in the "no compensation" data (blue markers); the same data are plotted with compensation for parasitic capacitance (green squares). To explain the origin of this discontinuity, Fig. 2(d) shows a simulation of the feedback-to-actuation voltage ratio (V_{fb}/V_{total}). In the absence of parasitic capacitance, this ratio should be proportional to frequency (dashed lines). In contrast, the solid lines include capacitive effects (resembling first-order high-pass filters). It can be seen from Fig. 2(d) that measurements made with R_{fb3} at 10 kHz will underestimate V_{fb}, leading to the discontinuity in Fig. 2(c).

We propose that instantaneous drop velocity is a useful feature to track because it provides a unique proxy that is inversely

related to the resistive forces opposing drop motion. Any local modifications to the device surface or insulator (e.g., through biofouling or dielectric damage) should manifest as changes in drop velocity. Fig. 3 demonstrates the capability of the DropBot system to extract instantaneous velocity from the derivative of the device capacitance with respect to time (described in the online supplementary material[26]). Fig. 3(b) shows representative velocity profiles for a drop of deionized (DI) water being actuated at 100, 130, and 150 V_{rms}. Actuation force is proportional to voltage squared (Eq. (1)), so we expect higher voltages to produce increased velocities. Fig. 3(c) demonstrates this trend over a range of voltages, showing an increasing peak velocity at driving voltages up to ~250 V_{rms}, after which the velocity appears to saturate at 70–80 mm/s. While it is possible that the peak velocity continued to increase beyond 80 mm/s for voltages greater than 250 V_{rms}, this could not be confirmed because of limitations of the current system. In any case, we observed successful drop movements for the full 50 repetitions for voltages up to and including 330 V_{rms}. Note that each data point represents the velocities of a fresh drop of DI water translated across an unused set of electrodes, minimizing evaporation and other potential cumulative effects between experiments.

At 350 V_{rms}, we observed an abrupt change in the voltage/velocity trend; Fig. 3(d) shows a gradual reduction in peak velocity on a single electrode over the course of 50 repetitions. We observed a similar effect on the other three electrodes and on multiple devices operated at this voltage (data not shown). This suggests that for moving DI water on a device of this composition, 350 V_{rms} represents an upper limit beyond which there is a rapid and irreversible degradation of device performance. Interestingly, the drop was successfully translated across all electrodes for the full 50 repetitions; however, by the end of the experiment, the velocity was greatly reduced (<10 mm/s). There was no measurable change in the capacitance of the dielectric, nor was there any evidence of
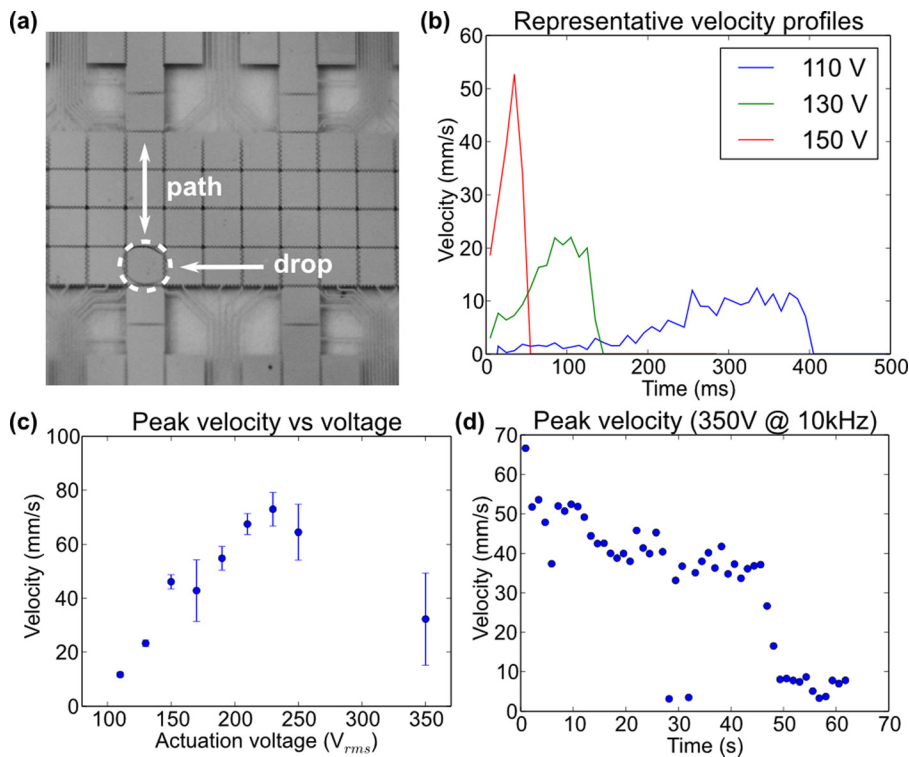
FIG. 3. Drop velocity measurements. (a) Video frame from a sequence showing a drop of water moving across four electrodes. (b) Representative instantaneous velocity profiles for a drop of water actuated at 110 (blue), 130 (green), and 150 V_{rms} (red) (frequency = 10 kHz) onto an electrode. (c) Average peak velocity of a drop of water moving over four electrodes 50 times at different actuation voltages (frequency = 10 kHz, error bars represent ± 1 S.D.). (d) Peak velocities from c shown for each of the 50 repetitions for the 350 V_{rms} experiment.

electrolysis, which suggests that this phenomenon was not driven by dielectric breakdown. The affected electrodes were qualitatively observed to be hydrophilic by running a stream of DI water over the device, consistent with suggestions in the electrowetting literature that excessive voltage causes surface modifications through air ionization.[24] Thus, we hypothesize that the voltage-induced surface modifications increased the resistive force on the drops. We suspect that this represents an additional mechanism beyond those commonly attributed to device failure (i.e., biofouling[6,7] and dielectric breakdown[25]), and we plan to investigate this effect in future work.

High-voltage amplifiers are often used for DMF with the assumption that they have constant gain—i.e., that they produce an output voltage that is a linear scaling of the input signal. But we report here that this assumption is often invalid, and in fact, DMF automation systems are frequently operated under conditions in which amplifier gain is unstable, causing unwanted and unpredictable changes in output voltage. Fig. 4(a) demonstrates that the Trek PZ700 amplifier used in our system has constant gain at frequencies below ~1 kHz; however, at higher frequencies (up to ~20 kHz is common for DMF) and as additional switching modules are added to the system, the behaviour changes dramatically, with output variations of up to $\pm 60\%$. This behaviour is expected for driving large capacitive loads and is not unique to this particular amplifier. In general, it is difficult to design amplifiers that can operate at (1) high frequency, (2) high voltage, and (3) drive large capacitive loads, making it likely that any amplifier used for DMF will be operated at or beyond its limits under certain experimental conditions. Fig. 4(b) shows that even the simple act of turning an electrode on/off can significantly change the output voltage.
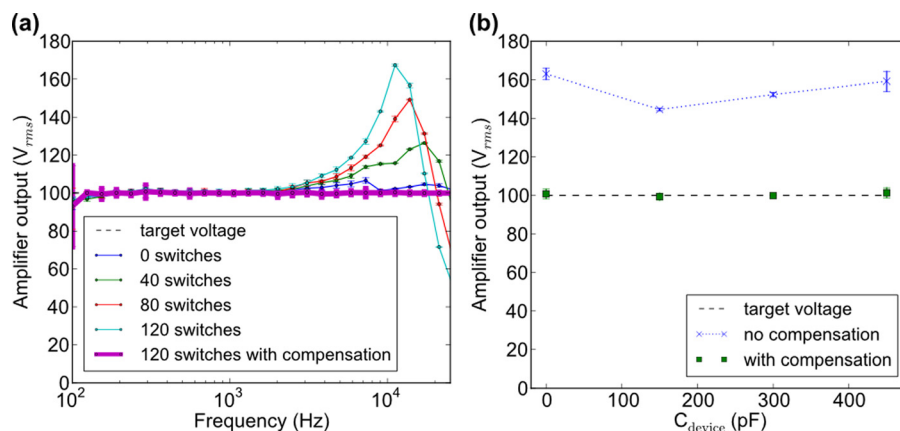

FIG. 4. Amplifier-gain compensation. (a) Amplifier output as a function of frequency for a target voltage of 100 V_{rms} with different numbers of solid-state switches (0-dark blue, 40-green, 80-red, 120-light blue) attached to the amplifier (all switches are in their off state). The magenta curve demonstrates the ability of the gain compensation feature to achieve a flat frequency response up to the maximum bandwidth of the amplifier (~20 kHz) with 120 switches attached. Error bars represent ± 1 S.D. from 10 replicate measurements. (b) Amplifier output voltage with gain compensation (green squares) and without (blue symbols) as a function of device capacitance for a frequency of 10 kHz. The ~0, 150, and 300, and 450 pF device loads are a result of actuating 0, 1, 2, or 3 reservoir electrodes each containing 10 μl. Error bars represent ± 1 S.D. from 100 replicate measurements.
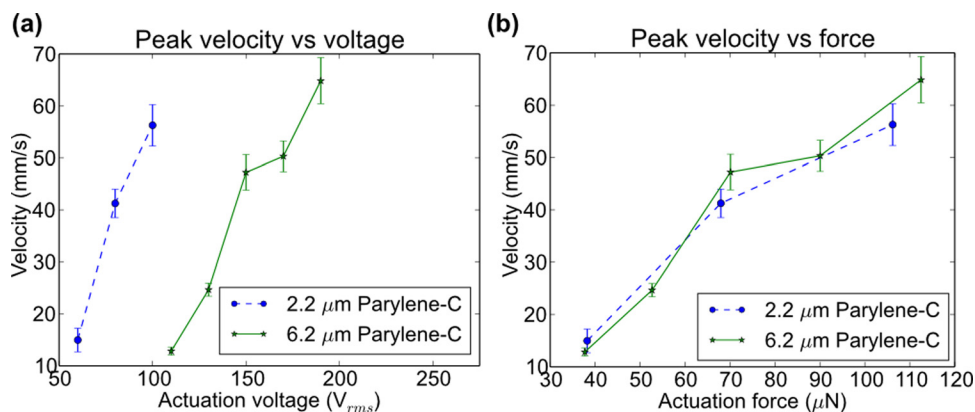
FIG. 5. Normalizing actuation voltage by electrostatic force. (a) Average peak velocity for a drop of water moving across the same electrode 50 times at different actuation voltages (frequency = 10 kHz, error bars represent ±1 S.D. from 50 measurements) for two thicknesses of Parylene-C (2.2 μm-blue and 6.2 μm-green). (b) Data from a plotted as a function of driving force as per Eq. (1).

To compensate for non-ideal amplifier behavior, the DropBot system was designed to monitor the amplifier output and adjust the input every 10 ms. Figs. 4(a) and 4(b) demonstrate the effectiveness of this approach for frequencies up to 20 kHz and with several reservoirs actuated simultaneously.

Although this compensation scheme is effective under typical operating conditions, there are other possible strategies for addressing amplifier-loading effects. One solution may be to redesign the switching boards to present a lower capacitive load to the amplifier. This could be achieved through a more optimal circuit board layout and/or by using relays with a lower off-state capacitance. It may also be possible to find a high-voltage amplifier with improved performance under high loads. For any given amplifier, the compensation scheme described here should enable stable operation at higher frequencies and/or higher loads than would be possible otherwise.

Small-batch, manual fabrication of DMF devices often results in loose tolerances over insulator thickness. This requires ad hoc adjustments to actuation voltage to achieve consistent drop movement across devices. Fig. 5(a) shows the peak velocity for drops of DI water driven with a range of actuation voltages on two DMF devices, each with a different thickness of Parylene-C. Note that the device with the 2.2 μm dielectric layer achieved equivalent peak velocities to the 6.2 μm layer device using much lower voltages. This is expected because actuation force is proportional to dielectric capacitance (Eq. (1)), and the thinner dielectric exhibits a higher capacitance per unit area. Because the DropBot system measures device capacitance and actuation voltage simultaneously, it can estimate the actuation force for any arbitrary device connected to the system. Fig. 5(b) demonstrates that when peak drop velocity is normalized by the estimated actuation force, the 2.2 and 6.2 μm devices are virtually indistinguishable. The capability to automatically apply a consistent actuation force regardless of the particular device characteristics is attractive from a user perspective, and is unique to the DropBot system. This feature also allows for meaningful comparisons of drop velocity between devices with varying dielectric properties.

In conclusion, we present DropBot, an open-source platform for controlling and characterizing DMF devices. We have demonstrated the system's ability to measure instantaneous drop velocity and to precisely control the applied electrostatic force through compensation for amplifier-loading

and parasitic capacitance. We believe that these combined features will be useful to end-users developing new assays or characterizing and optimizing device design and control. We further suggest that the quantitative metrics provided by this system will be useful for addressing some of the outstanding challenges in the field, including improved device robustness and resistance to biofouling.

[1]M. G. Pollack, R. B. Fair, and A. D. Shenderov, Appl. Phys. Lett. **77**, 1725 (2000).

[2]M. G. Pollack, A. D. Shenderov, and R. B. Fair, Lab Chip **2**, 96 (2002).

[3]H. M. Cho and C.-J. Kim, J. Microelectromech. Syst. **12**, 70 (2003).

[4]R. Fair, Microfluid. Nanofluid. **3**, 245 (2007).

[5]K. Choi, A. H. C. Ng, R. Fobel, and A. R. Wheeler, Annu. Rev. Anal. Chem. **5**, 413 (2012).

[6]V. N. Luk, G. C. Mo, and A. R. Wheeler, Langmuir **24**, 6382 (2008).

[7]S. H. Au, P. Kumar, and A. R. Wheeler, Langmuir **27**, 8586 (2011).

[8]S. C. C. Shih, R. Fobel, P. Kumar, and A. R. Wheeler, Lab Chip **11**, 535 (2011).

[9]S. C. C. Shih, H. Yang, M. J. Jebrail, R. Fobel, N. McIntosh, O. Y. Al-Dirbashi, P. Chakraborty, and A. R. Wheeler, Anal. Chem. **84**, 3731 (2012).

[10]Y.-J. Shin and J.-B. Lee, Rev. Sci. Instrum. **81**, 014302 (2010).

[11]K. S. Elvira, R. Leatherbarrow, J. Edel, and A. deMello, Biomicrofluidics **6**, 022003 (2012).

[12]S. C. C. Shih, I. Barbulovic-Nad, X. Yang, R. Fobel, and A. R. Wheeler, Biosens. Bioelectron. **42**, 314 (2013).

[13]H. Ren, R. B. Fair, and M. G. Pollack, Sens. Actuators B **98**, 319 (2004).

[14]J. Gong and C.-J. Kim, Lab Chip **8**, 898 (2008).

[15]M. J. Schertzer, R. Ben-Mrad, and P. E. Sullivan, Sens. Actuators B **145**, 340 (2010).

[16]T. Lederer, S. Clara, B. Jakoby, and W. Hilber, Microsyst. Technol. **18**, 1163 (2012).

[17]H. Ding, S. Sadeghi, G. J. Shah, S. Chen, P. Y. Keng, C.-J. Kim, and R. M. van Dam, Lab Chip **12**, 3331 (2012).

[18]S. Sadeghi, H. Ding, G. J. Shah, S. Chen, P. Y. Keng, C.-J. Kim, and R. M. van Dam, Anal. Chem. **84**, 1915 (2012).

[19]B. Hadwen, G. R. Broder, D. Morganti, A. Jacobs, C. Brown, J. R. Hector, Y. Kubota, and H. Morgan, Lab Chip **12**, 3305 (2012).

[20]M. A. Murran and H. Najjaran, Lab Chip **12**, 2053 (2012).

[21]T. B. Jones, K.-L. Wang, and D.-J. Yao, Langmuir **20**, 2813 (2004).

[22]D. Chatterjee, H. Shepherd, and R. L. Garrell, Lab Chip **9**, 1219 (2009).

[23]S.-K. Fan, Y.-W. Hsu, and C.-H. Chen, Lab Chip **11**, 2500 (2011).

[24]M. Vallet, M. Vallade, and B. Berge, Eur. Phys. J. B **11**, 583 (1999).

[25]J. H. Song, R. Evans, Y.-Y. Lin, B.-N. Hsu, and R. B. Fair, Microfluid. Nanofluid. **7**, 75 (2009).

[26]See supplementary material at http://dx.doi.org/10.1063/1.4807118 for detailed experimental methods.